Hybrid Cartesian/unstructured numerical method for efficient evaluation of scattered fields: Application to buried object detection from airborne platforms

Lisa-marie Mazzolo, Xavier Ferrieres

Received: 21 December 2023 | Revised: 2 May 2024 | Accepted: 26 June 2024

DOI: 10.1002/jnm.3270

RESEARCH ARTICLE

WILEY

Hybrid Cartesian/unstructured numerical method for efficient evaluation of scattered fields: Application to buried object detection from airborne platforms

Lisa-Marie Mazzolo[1] | **Xavier Ferrieres**[2]

[1]Electromagnetism and Radar Department, ONERA, Salon-de-Povence, France

[2]Electromagnetism and Radar Department, ONERA, Université de Toulouse, Toulouse, France

Correspondence
Lisa-Marie Mazzolo, Electromagnetism and Radar Department, ONERA, F-13661 Salon cedex Air, France.
Email: lisa-marie.mazzolo@onera.fr

Xavier Ferrieres, Electromagnetism and Radar Department, ONERA, Université de Toulouse, F-31000 Toulouse, France.
Email: xavier.ferrieres@onera.fr

Abstract

This paper focuses on the study and development of an efficient numerical method designed to simulate the radar cross section (RCS) of objects buried in lossy ground and illuminated by a plane wave. The primary objective aligns with the overarching challenge of detecting buried targets in the ground using an airborne radar system. In this scenario, a source antenna illuminates a considered 3D domain, and sensors receive the scattered field from the targets. To enable accurate and efficient simulations, the proposed tool utilizes a Cartesian/unstructured mesh and employs hybrid method that combines two finite volume solvers. In the contents of the paper, we first present a strategy for obtaining Cartesian/unstructured meshes. Subsequently, we study the hybridization of two specific finite volume schemes. Additionaly, a ground and a Near- to Far-field model are introduced for buried targets. To validate and showcase the advantages of our hybrid approach, practical examples are presented. Finally, the strategy designed for handling meshes composed of multiple Cartesian and unstructured zones is detailed.

KEYWORDS

buried objects, finite volume methods, hybrid Cartesian/unstructured mesh generation, Maxwell equations, RCS simulation, scheme hybridization

1 | INTRODUCTION

The growing concern in the study of system electromagnetic (EM) environment is frequently dealt with simulation tools. In this paper, we are especially interested in remote sensing problem staging airborne source and sensor. In the context of buried object detection, efficient numerical simulations can indeed be beneficial, by helping to predict the expected scattering response of the buried target and thus allowing an a priori evaluation of the detection capabilities.

Due to the increasing complexity of structures, more and more efficient simulation methods are required. For evaluating the scattered fields (SFs) from objects buried in a lossy medium, previous studies[1–3] have used the ubiquitous

Yee's scheme[4] based on finite difference time domain technique (FDTD).[5] However, despite its efficiency and robustness, this method is limited by the use of Cartesian grids (ST*), so it requires a high level of discretization to accommodate objects with curved parts, which increases the computational cost. Alternative approaches such as the finite volume time domain (FVTD) scheme[6–8] using unstructured meshes (UNST) provide better geometric representations. Moreover, when dealing with simulations involving buried objects, it is necessary to account for multiple media characterized by diverse propagation speeds. The FVTD scheme exhibits the capability to manage meshes featuring locally refined cells of varying sizes, specifically designed to accommodate these distinct velocity media. Nevertheless, the computation of EM fields by this method generally requires higher computation time and storage capacities than the FDTD approach. Thus, to improve the modeling capabilities, a natural idea is to employ hybrid ST/UNST grids coupled with a hybrid FDTD/FVTD scheme.[9,10] This involves meshing the computational domain using a Cartesian grid with locally unstructured mesh areas (around curved surfaces) and applying FDTD on the Cartesian part and FVTD on the unstructured part. However, the stability of hybrid FDTD/FVTD-UNST strategy is not clearly demonstrated for the most of the solutions proposed so far and is consequently still rarely used.

Our objective is to propose a new stable hybrid method for solving unsteady Maxwell's equations, in order to deal with remote sensing problems. In pursuit of this, our focus lies on hybridization based on finite volume approaches in which stability is ensured. Then, we suggest to apply an FVTD-USNT scheme on unstructured part and a less ressource-intensive FVTD-ST scheme on remaining computational domain. We chose FVTD schemes that, according to us, provide the most efficient solutions both in the ST- and UNST-parts. This strategy additionally allows for the possibility of locally refining specific sections within these hybrid meshes.

This paper is organized as follows. In Section 2, we present the hybrid ST/UNST mesh generation strategy. Moving on to Section 3, we formulate and study a hybrid FVTD-ST/UNST technique. We start by presenting the general principle of the finite volume method. Following this, we introduce the chosen FVTD-ST scheme, designed to manage the ST-part of our hybrid meshes. Subsequently, we focus on the more-ressource intensive FVTD-UNST scheme, capable of handling the UNST-part or entire hybrid ST/UNST meshes. To reduce the computation cost of this approach, we introduce and discuss two strategies: variable approximation order and local time stepping. These strategies are tested through numerical examples, considering a hybrid ST/UNST mesh representing a PEC (perfect electric conductor) sphere in free space. Next, in Section 3.4, we explain the implementation principle of the hybrid FVTD-ST/UNST method and evaluate its capabilities through numerical results, still considering our free-space hybrid sphere mesh. We especially highlight the existing and prospective benefits of the hybrid FVTD-ST/UNST approach in comparison to pure FDTD or FVTD methods. Additionally, in Section 4, we focus on evaluating SFs from a buried object in a lossy medium, particularly in the context of simulating airborne radar measurements. We introduce established models from the existing literature, into our finite volume approach, specifically designed to handle scenarios involving a ground, with transmitters and receivers positioned far away from the air-ground interface. We also discuss the advantages of using locally refined meshes and examine the challenges associated with utilizing the hybrid FVTD-ST/UNST scheme. Finally, we conclude with reflections on the method's applicability and offer suggestions for future work.

2 | GENERATION OF HYBRID CARTESIAN/UNSTRUCTURED MESHES

Cartesian meshes are easier to implement and process but curved surfaces are approximated using “stair-cased” representations. In UNST meshes, curves are properly accommodated using body-fitted meshes, though more complex to generate and implement. Therefore in our study, we aim to make the most of both methods and generate hybrid ST/UNST grids to reduce computational cost (reducing the number of UNST cells) while preserving correct consideration of the geometry.

The principle of our hybrid grid generation strategy includes several steps that can be performed automatically. Considering an object with curved surfaces, these generation steps are as follows:

1. Generate a triangular surface mesh for the considered object. We have developed specific tools for this purpose, but open-source software such as GMSH[11] is also applicable.

*In this paper, the abbreviation ‘ST’ is intentionally used to refer to Cartesian meshes, to echo the abbreviation“UNST” for unstructured.

2. Generate a Cartesian mesh adapted to the 3D computational domain, and immerse the object generated in the first step. Define a global object area in the Cartesian mesh, corresponding to the object enclosed by a specific volume (the future unstructured part).
3. Create a surface mesh of triangular elements at the boundary between the global object area and the Cartesian mesh. Generate an unstructured tetrahedral volume mesh between the surface meshes of the object and the Cartesian/global object area boundary.
4. Finally, merge the Cartesian mesh and the UNST-part of the global object area to generate the hybrid mesh.

Resulting hybrid mesh can be seen as a Cartesian mesh in which an unstructured part is included around the object of interest. Figure 1 shows an example of a hybrid mesh with a spherical object. The unstructured mesh is composed of either tetrahedral cells or polyhedral cells with more than six faces. There is specific UNST cells with a particular geometry lay at the interface: a rectangular surface on one side to connect to the Cartesian part of the mesh, and a split surface with two triangles to match tetrahedral cells on the other one (Figure 2). This kind of hybrid grids can be used without difficulty with an FVTD technique. Indeed, the principle of the FVTD method is based on the exchange of fluxes through the interfaces of the volume cells.

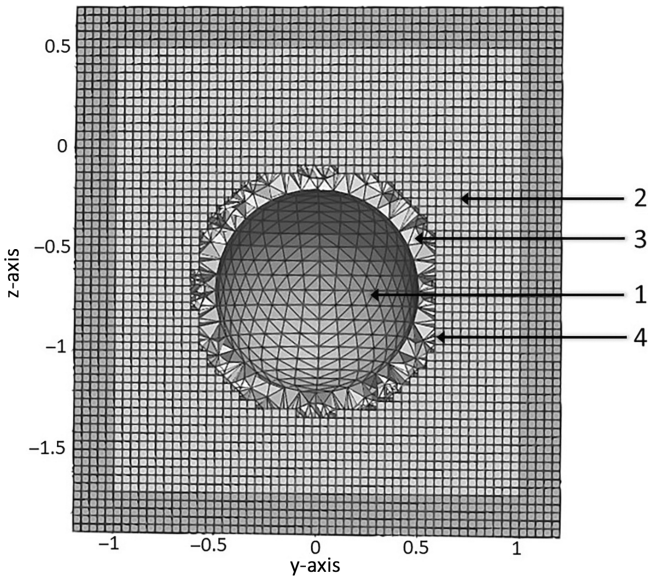

FIGURE 1 Cross section of a Hybrid ST/UNST grid perpendicular to *x*-axis and generation steps. Step 1: Surface mesh of a sphere. Step 2: External Cartesian volume mesh. Step 3: UNST volume mesh between the sphere and Cartesian boundary surface meshes. Step 4: Final hybrid mesh.

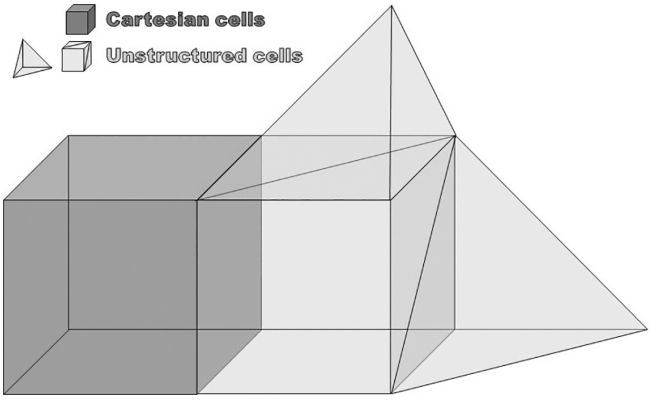

FIGURE 2 Cell hybridization interface between a Cartesian mesh and an unstructured mesh.

3 | HYBRID FINITE VOLUME ON CARTESIAN/UNSTRUCTURED MESH METHOD

The FVTD method is a flexible numerical scheme based on differential equations, used for simulating 3-D EM problems.[6–8] Unlike the FDTD method, FVTD-UNST techniques can support meshes with cells of different shapes and then correctly accommodate curved geometries but require a higher computational cost. Thus, considering hybrid meshes, a practical approach to achieving accurate solutions while minimizing computational cost is to combine two finite volume methods. The idea is to exclusively apply the more ressource intensive FVTD-UNST method to the UNST-part and utilize another less costly scheme on the ST-part, such as an appropriate FVTD-ST scheme. We actually propose a hybridization of meshes associated with a hybridization of numerical schemes. In this section, following the introduction of the general principle of the finite volume scheme, we present and compare two implementations of FVTD methods, one on ST meshes and the other on UNST meshes.

3.1 | General principle of the finite volume scheme

The general principle of the FVTD method consists in solving the conservative form of Maxwell's equations on each elementary cell that can be written as:

$$\frac{\partial U}{\partial t}+\nabla\times F(U)=0, \tag{1}$$

where $U=\left(E_x,E_y,E_z,H_x,H_y,H_z\right)^T$ and

$$F(U)=\begin{pmatrix}\begin{pmatrix}0\\ \frac{H_z}{\epsilon_0}\\ -\frac{H_y}{\epsilon_0}\\ 0\\ -\frac{E_z}{\mu_0}\\ \frac{E_y}{\mu_0}\end{pmatrix} & \begin{pmatrix}-\frac{H_z}{\epsilon_0}\\ 0\\ -\frac{H_x}{\epsilon_0}\\ \frac{E_z}{\mu_0}\\ 0\\ -\frac{E_x}{\mu_0}\end{pmatrix} & \begin{pmatrix}\frac{H_y}{\epsilon_0}\\ -\frac{H_x}{\epsilon_0}\\ 0\\ -\frac{E_y}{\mu_0}\\ \frac{E_z}{\mu_0}\\ 0\end{pmatrix}\end{pmatrix},$$

where ϵ_0 and μ_0, the electric permittivity and magnetic permeability of free space. Integrating (1) over the volume V of a computation domain cell yields:

$$\frac{\partial}{\partial t}\int_V UdV+\int_S F(U^*)\cdot ndS=0, \tag{2}$$

where $U^*=(E^*,E^*)^T$. E^* and E^* represent the values of E and H on the surface s with unit normal vector n pointing outward from volume V. The numerical flux $F(U^*)$ is defined as $((n\times H^*)/\epsilon_0,-(n\times H^*)\mu_0)^T$. In this paper, only cell-centered FVTD schemes are considered to evaluate the field components. In each cell, electric field E and magnetic field H are computed at the center of gravity of that respective cell. After discretization of the computational domain, we obtain for each cell of volume V_i:

$$V_i\frac{\partial U_i}{\partial t}=-\sum_{l=1}^{N_s}S_lF\left(U_l^*\right)n_l, \tag{3}$$

where N_s denotes the number of surface S_l bounding the cell i, and n_l represents the outward unit normal vector to the surface S_l. Therefore, to compute fields at the center of the cells, it is necessary to evaluate numerical fluxes on their

boundary surfaces. To achieve this, we use the field values from the volumes adjacent to the considered cell. Specifically, to approximate numerical fluxes ($n \times H^*$ and $n \times E^*$) in free space at the interface between two volumes V_L and V_R, we utilize tangential continuity of the fields and characteristic equations as described by Bonnet et al.,[7] to obtain:

$$n \times H^* = \frac{1}{2}\left(n \times \left(H^R + H^L\right) + \sqrt{\frac{\epsilon_0}{\mu_0}} n \times n \times \left(E^R - H^L\right)\right), \tag{4}$$

$$n \times E^* = \frac{1}{2}\left(n \times \left(E^R + E^L\right) + \sqrt{\frac{\mu_0}{\epsilon_0}} n \times n \times \left(H^R - H^L\right)\right), \tag{5}$$

where E^L and H^L represent the electric and magnetic field values at the center of volume V_L and E^R and H^R field values at the center of volume V^R.

3.2 | Finite volume method on Cartesian mesh (FVTD-ST method)

In this subsection, we provide the FVTD scheme that will be applied to the ST-part of our hybrid mesh. Utilizing the general principle of the finite volume method outlined earlier, we delve into the chosen numerical flux approximation in this scheme. To minimize the computational cost, we opt for a noncentered Godunov's approximation and incorporate a γ parameter to weight dissipation ($\gamma \epsilon [0,1]$). This approach represents a simplified version of the $\beta\gamma$ approximation, where the arguments in the flux definition are replaced with extrapolated arguments involving gradients from adjacent cells and a weighting factor β to minimize dispersion.[12] In the context of implementation within our hybridization strategy, based on our numerical experiments, we find it is unnecessary to complicate the flux calculation using the $\beta\gamma$ method to increase the order of approximation.

Finally, to calculate fluxes in free space at the interface between two volumes V_L and V_R, we introduce only the additional parameter γ into to (4) and (5) as follows:

$$n \times H^* = \frac{1}{2}\left(n \times \left(H^R + H^L\right) + \gamma\sqrt{\frac{\epsilon_0}{\mu_0}} n \times n \times \left(E^R - H^L\right)\right), \tag{6}$$

$$n \times E^* = \frac{1}{2}\left(n \times \left(E^R + E^L\right) + \gamma\sqrt{\frac{\mu_0}{\epsilon_0}} n \times n \times \left(H^R - H^L\right)\right). \tag{7}$$

The use of Cartesian meshes, where cells are indexed by (i, j, k), simplifies flux computation and does not require the storage of flux quantities. For the cell (i, j, k), the time derivative of magnetic component H_x can be thus written as follows:

$$\frac{\partial H_x}{\partial t}(i,j,k) = -\frac{1}{\mu_0}\left(\frac{\left(n_{-y} \times E^*\left(i,j-\frac{1}{2},k\right)\right)_x}{\partial y} + \frac{\left(n_{+y} \times E^*\left(i,j+\frac{1}{2},k\right)\right)_x}{\partial y} + \frac{\left(n_{-z} \times E^*\left(i,j,k-\frac{1}{2}\right)\right)_x}{\partial z} + \frac{\left(n_{+z} \times E^*\left(i,j,k+\frac{1}{2}\right)\right)_x}{\partial z}\right), \tag{8}$$

where $()_x$ denotes the x_component and $n_{\pm y}$, $n_{\pm z}$ represent unit normal vectors at the specified boundary surfaces of cell (i,j,k), expressed in the Cartesian basis (x, y, z). Considering the interface $(i, j-1/2, k)$, we have:

$$\left(n_{-y} \times E^*\left(i,j-\frac{1}{2},k\right)\right)_x = \frac{E_z(i,j-1,k) + E_z(i,j,k)}{2} - \frac{\gamma}{2}\mu_0 c_0 \left(H_x(i,j,k) - H_x(i,j-1,k)\right), \tag{9}$$

where $c_0 = 1/\sqrt{\epsilon_0\mu_0}$, the speed of light in the medium. In the case of the interface between $(i, j+1/2, k)$:

$$\left(n_{+y}\times E^{*}\left(i,j+\frac{1}{2},k\right)\right)_{x}=\frac{-E_z(i,j+1,k)-E_z(i,j,k)}{2}-\frac{\gamma}{2}\mu_0 c_0\left(H_x(i,j,k)-H_x(i,j+1,k)\right) \tag{10}$$

Fluxes are expressed in an analogous way on each interface.

Note that by setting $\gamma = 0$, we obtain a centered Godunov approximation. A value of γ that is too high results in excessive dissipation, while an excessively low value, although reducing dissipation, leads to parasitic oscillations characteristic of centered fluxes.[12]

For temporal discretization, we use an explicit leap-frog scheme. The time step dt_{ST} should satisfy a CFL criterion given, in free space, by[13]:

$$dt_{ST} \leq \frac{d_l}{c_0}, \tag{11}$$

where d_l denotes the spatial step size.

3.3 | Finite volume method on unstructured mesh (FVTD-UNST method)

In contrast to the previous Cartesian approach, utilizing unstructured meshes complicates the computation of numerical fluxes, leading to a higher computational cost. This complexity arises because evaluating fluxes necessitates storing field values and related information for each adjacent cell. Consequently, the FVTD-UNST scheme requires more memory than the FVTD-ST technique. Additionally, to ensure the stability of the FVTD-UNST scheme, the time step dt_{UNST} must satisfy the following nonoptimal CFL condition[14]:

$$dt_{\mathrm{UNST}} \leq \min_{k=1,N_V} \frac{1}{c_0}\frac{V_k}{\Sigma_{l=1}^{N_S} S_l}, \tag{12}$$

where N_V is the number of cells in the computational domain and N_S the number of surfaces S_l that enclose the volume V_k.

Therefore, the time step could be very small, as it needs to correspond to that of the smallest cell. This requirement can be constraining and costly for the computation.

In the following Section 3.3.1, we introduce two options to overcome these constraints and reduce the computation time: variable approximation order and local time stepping strategies. Subsequently, in Section 3.3.2, we provide examples in free space illustrating the advantages of both strategies.

3.3.1 | Variable approximation order and local time stepping strategies

The variable approximation order consists in choosing a local flux approximation, which depends on cell size. We opt for a GODUNOV scheme (spatial order 0) for the smallest cells and a MUSCL scheme[15] (spatial order 1) for the other cells. The latter requires evaluating internal gradients for each field component, that is 18 additional unknows, and consequently increasing the computational cost. Therefore, limiting the use of MUSCL scheme to specific cells reduces the computation of gradients, lowering both computational cost and memory requirements. We consider, based on our numerical experiments, that the approximation using a Godunov scheme is sufficiently accurate for cells with dimensions $d_r < \lambda/30$, where d_r denotes the radius of the circle within which the considered cell is inscribed and λ the wavelength.

The second improvement option involves introducting local time stepping instead of using a single global time step for the entire simulation. A minimum time step $dt_{\min}$ and a maximum time step $dt_{\max}$ are computed based on cell size. The global time step dt_{UNST} is not simply the previously calculated minimum time step. Instead, N cell classes are defined, and for each class N_i, a local time stepping is computed:

$$dt_{loc}^{N_i} = 3^{N_i-1} dt_{\min}. \tag{13}$$

The global time step dt_{UNST} is then set as the maximum among the computed local time steps, as follows:

$$dt_{UNST} = 3^{N-1} dt_{min} \tag{14}$$

In each time iteration, fields for each cell class N_i are computed recursively at their respective local time steps until reaching the global time. The use of local time stepping enables varying computation times for different cell class, rather than employing the smallest time step $dt_{\min}$ for all cells. This approach ultimately results in a significant reduction in central processing unit (CPU) time.

3.3.2 | Numerical examples in free space

We conducted tests on a hybrid ST/UNST mesh representing a PEC sphere with a radius of 0.5 m in free space (Figure 1). The input waveform's time function is defined as a Gaussian pulse: $E_x = A_{\exp}\left(\frac{-(t-t_0)^2}{b^2}\right)$, with $A = 1$, $t_0 = 10$ ns and $b = 1$ ns. The constants were chosen to ensure sufficient energy propagation within the frequency range of interest, specifically ranging from 100 to 500 MHz ($\lambda_{\min} = 3$m, $\lambda_{\max} = 0.6$m). The incident wave is introduced using the SF formulation.[1] The computational space is a rectangular cuboid of dimensions 2.4m × 2.4m × 2.6m, within which five absorbing layers, also known as PML (perfectly matched layer),[16] were introduced in each direction ($\pm x$, $\pm y$, $\pm z$). ST cells have edges of $d_l^H = 0.04$m ($\approx \lambda_{\max}/15$), and UNST cells for surface mesh object have edges of $a = 0.08$m ($\approx \lambda_{\max}/8$). We computed the backscattered radar cross section (RCS) as function of frequency, using our stand-alone FVTD-UNST method, both with and without local approximation order, as well as with and without the local time stepping. The RCS of a target is a property that can be analytically computed for a PEC sphere using Mie series.[17] Therefore, we can validate our results using the solution provided by the RCSsphere MATLAB function from the Radar Toolbox,[18] represented in black in Figure 3.

To highlight the advantages of variable approximation order, we conducted three simulations employing local time stepping with a GODUNOV approximation, a MUSCL approximation and variable order. In the case of the latter, flux approximation was carried out using the GODUNOV's method for 2761 cells and the MUSCL approach for 221939 cells. The results in Figure 3 indicate that the solutions provided by the MUSCL approximation alone and the variable approximation order are nearly identical and closest to the analytical solution. In contrast, the solution from the

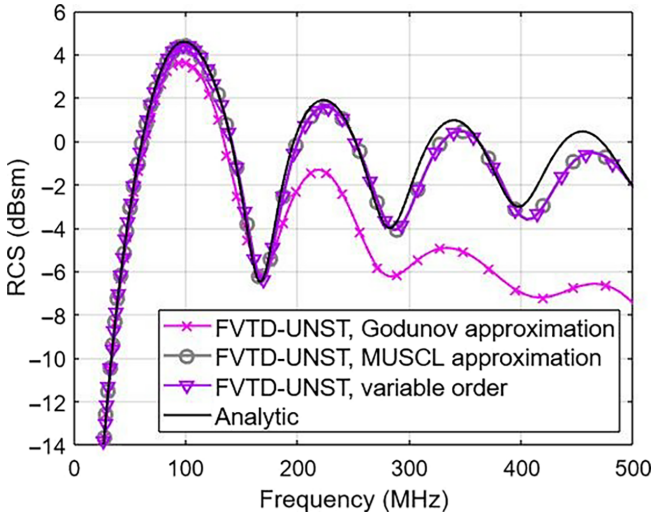

FIGURE 3 Sphere RCS as function of frequency, computed using FVTD-UNST simulations with different numerical flux approximations.

GODUNOV's method alone deviates significantly from the analytical solution, especially at higher frequencies. Additionally, employing variable approximation order reduces computation time compared with a MUSCL scheme alone (Table 1). Therefore, using variable-order for flux approximation based on cell size enhances accuracy compared with a uniform Godunov's approach and saves time over a MUSCL approximation alone.

Then, we conducted two simulations with variable approximation order: one without local time stepping and the other with it. In the first approach, considering the hybrid mesh used, the global time step dt_{UNST} was 2.1629×10^{-12} s. However, in the second approach, we defined three cell classes (Table 2) and the global time step dt_{UNST} was set to 1.9466×10^{-11} s. For similar solutions, the computation time for the simulation without local time stepping is 6.4 times higher than the computation time for the simulation with local time step. This clearly demonstrates significant improvements achieved by implementing local time stepping. Given these results, the two proposed strategies will lead to a much more efficient scheme in terms of CPU time.

3.4 | Hybrid FVTD-ST/UNST scheme

The proposed hybrid method, combining FVTD-ST and FVTD-UNST techniques does not encounter stability problems because the use of two types of finite volume methods ensures consistent numerical fluxes at interfaces. Stability is not easily guaranteed with other hybrid approaches, such as FDTD/FVTD-UNST hybridization.[10]

In our hybridization process between the FVTD-ST and FVTD-UNST schemes, a global time step needs to be defined. However, time steps in ST- and UNST-parts are not necessarily identical. Consequently, the global time step dt_{global} used for the complete simulation is chosen as the minimum between the time steps of the ST- and UNST-parts to ensure the stability. The hybridization is performed on a free space interface. Time iterations are performed on the global time step and the computations for the ST- and UNST-parts are performed on separate CPUs. In each time iteration within the UNST-part, fields for each cell class are computed recursively at each local time step until reaching the global time. Electric and magnetic field information is then exchanged between the finite volume schemes at time meeting points (Figure 4).

Our objective was to compare the efficiency of our hybrid method with that of our FVTD-UNST, FVTD-ST (with parameter $\gamma = 0.01$) techniques, as well as the classic FDTD scheme. To achieve this, we applied our hybrid method to the hybrid sphere mesh used previously to test the stand-alone FVTD-UNST approach. We then applied FVTD-ST (with parameter $\gamma = 0.01$), FDTD techniques on a Cartesian mesh equivalent to the hybrid mesh, with ST cells having edges of length $d_l^C = 0.04$m. The results of these simulations are shown in Figure 5. It is obvious that the solution closest to the analytical solution is achieved with unstructured finite volume approach on the hybrid mesh, still represented in dark blue. However, despite the improvements made through the use of variable approximation order and local time stepping, the computation time is significantly higher compared with finite difference or finite volume techniques on Cartesian meshes.

The hybrid solution is relatively similar to the FVTD-UNST one, but it is critical to note that the hybrid method offers a significant computational time advantage due to the reduced number of operations in ST-part (Table 3). While

TABLE 1 Gain in central processing unit (CPU) times compared to that obtained with variable approximation order (T_{vo}^{CPU}) for FVTD-UNST computations on hybrid mesh, depicting a PEC sphere in free space, with varying numerical flux approximations.

Approximation type	GODUNOV	MUSCL
CPU time	0.4 T_{vo}^{CPU}	1.1 T_{vo}^{CPU}

TABLE 2 Distribution of mesh cells into three classes and their corresponding local time steps.

Class	Number of cells per class	dt_{loc}
1	1133	2.1623×10^{-12} s
2	17 657	6.4886×10^{-12} s
3	205 910	1.9466×10^{-12} s

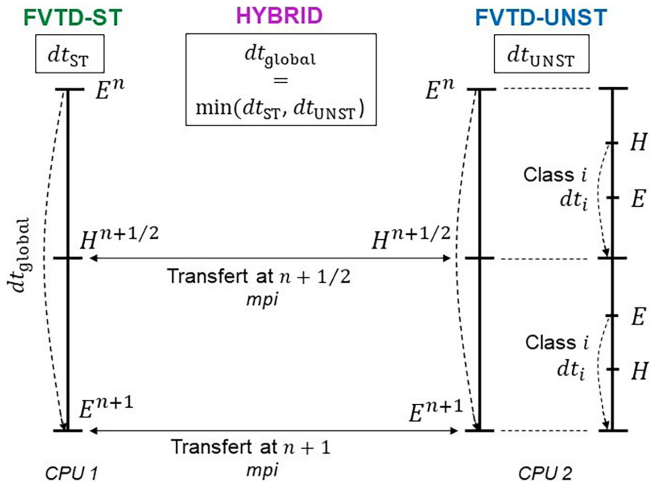

FIGURE 4 Diagram explaining the Hybrid method: FVTD-UNST and FVTD-ST field computations carried out separately, with field information exchanged.

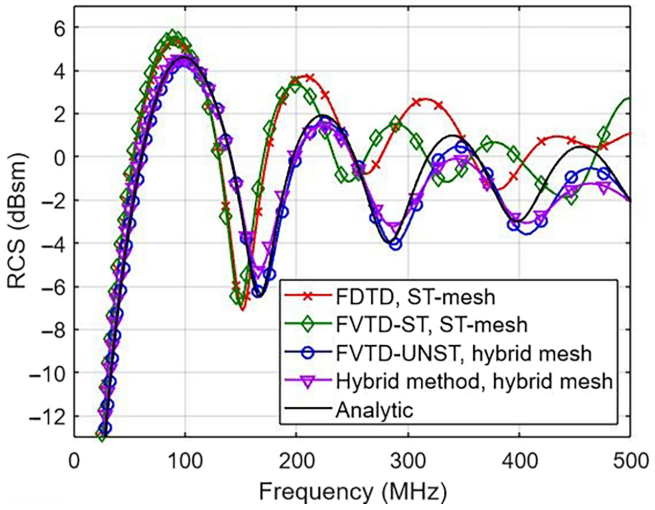

FIGURE 5 Sphere RCS as function of frequency obtained from FDTD, FVTD-ST, FVTD-UNST, and hybrid FVTD-ST/UNST computations.

TABLE 3 Gain in central processing unit (CPU) times for RCS computations of a PEC sphere in free space using FVTD-ST schemes on a Cartesian mesh, the FVTD-UNST scheme and the hybrid FVTD-ST/UNST method on a hybrid mesh, compared to that obtained with FDTD on a Cartesian mesh (T^{CPU}_{FDTD}).

	FVTD-ST	FVTD-UNST	Hybrid Method
CPU time	2.5 T^{CPU}_{FDTD}	158.5 T^{CPU}_{FDTD}	54.7 T^{CPU}_{FDTD}

the results are satisfactory, we do notice some attenuation and dispersion for higher frequencies compared to the analytical solution.

In our investigation, we set out to determine whether the issue stemmed from employing an excessively large spatial step. To assess this, we started by reducing the cell edge size a of the UNST surface mesh of the sphere by a factor of 2 ($\approx \lambda_{\max}/15$ instead of $\approx \lambda_{\max}/8$). As we can see in Figure 6, this does not improve the results and increases the computation time by a factor of 1.4. From these results, we note that an edge size a of 0.08 m for the UNST surface mesh is sufficient for achieving a conformal representation of the sphere. However, it does not prevent dispersion and attenuation at higher frequencies.

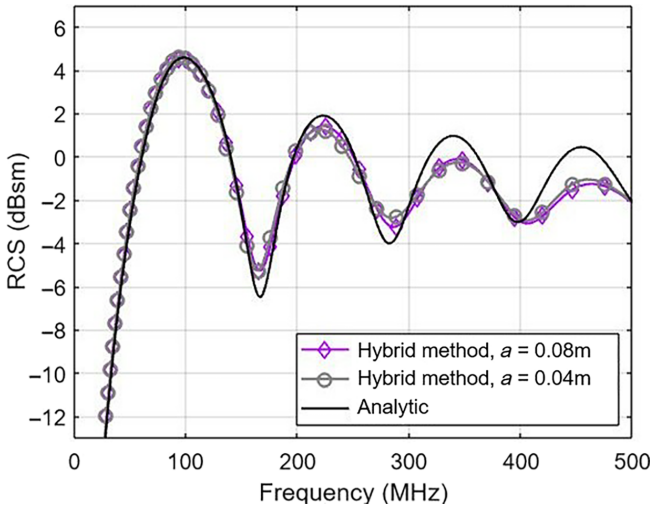

FIGURE 6 Sphere radar cross section (RCS) as function of frequency, computed using hybrid FVTD-ST/UNST simulations with varying cell edge size a of the sphere surface mesh.

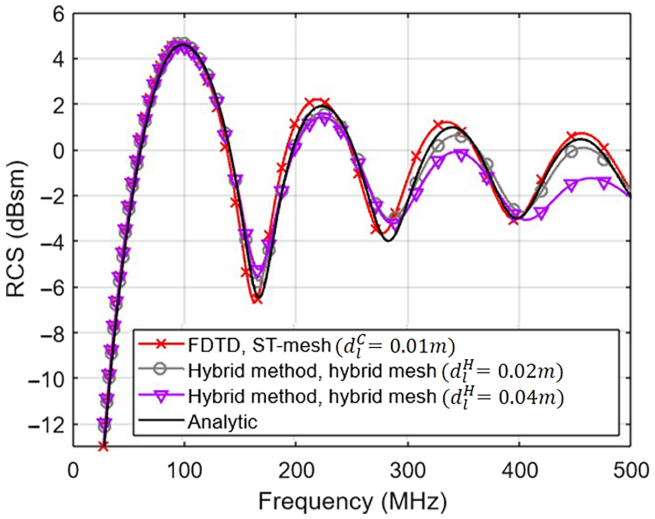

FIGURE 7 Sphere radar cross section (RCS) as function of frequency: Results obtained from FDTD computations on Cartesian mesh and hybrid FVTD-ST/UNST computations on two different hybrid meshes.

TABLE 4 Gain in central processing unit (CPU) times for radar cross section computations of a perfect electric conductor sphere in free space using the finite difference time domain technique (FDTD) scheme on Cartesian mesh with cell edge size d_l^C, and hybrid FVTD-ST/UNST method on a hybrid mesh with cell edge size $d_l^H = 0.2$m in the ST-part, compared to that obtained with hybrid FVTD-ST/UNST method (T_{Hyb}^{CPU}) on a hybrid mesh with cell edge size $d_l^H = 0.4$m in ST-part.

	FDTD	Hybrid FVTD-ST/UNST method
	$d_l^C = 0.01$m	$d_l^H = 0.02$m
CPU time	3.6 T_{Hyb}^{CPU}	5.3 T_{Hyb}^{CPU}

We then reduce the cell edge size d_l^H of the ST-part by a factor of 2 ($\approx \lambda_{\max}/30$ instead of $\approx \lambda_{\max}/15$). This time, as can be seen in Figure 7, the results are improved and fit in better with the analytical solution, but with a higher computational time (Table 4).

We also aimed to determine if FDTD method with a finer mesh provide better results than our hybrid approach. To assess this, we need to reduce the cell edge size d_l^C of the Cartesian mesh by a factor of 4, giving a cell edge size of

$d_l^C = 0.01\text{m}$ ($\approx \lambda_{\max}/60$ instead of $\approx \lambda_{\max}/15$). The number of cells is then multiplied by 4^3. The corresponding solution is shown in Figure 7. We observe that indeed, the FDTD method produces a result closer to the analytical solution, but with higher computational time and higher memory requirements compared with our hybrid method with four times larger cell edges in the ST-part (Table 4). However, it must be acknowledged that we need to decrease the mesh size in the ST-part to 0.02 m to achieve a hybrid solution close to that of the finite difference method, leading to higher computational costs in the end. Nevertheless, in light of our ongoing work, there is room for improvement in our hybrid FVTD-ST/UNST method. Indeed, it is not fully optimized in terms of the number of operations per iteration, especially regarding the FVTD-ST scheme and regarding computations within the PML. Moreover, in complex scenarios, especially those involving multi-layered ground with varying wave propagation speeds, our hybrid method and meshes are positioned to outperform traditional approaches. Indeed, when employing Cartesian meshes, variations in ground permittivity may require finer meshing, increasing the number of cells in the entire computational domain. In contrast, hybrid meshes allow us to consider cell nonconformity, and local refinement areas, thereby limiting the number of cells in the computational domain. Consequently, our hybrid method is expected to yield more efficient and accurate solutions compared with finite difference or finite volume methods used stand-alone on Cartesian meshes, while maintaining a lower computational cost than using FVTD-UNST method stand-alone on a hybrid mesh.

4 | SIMULATIONS OF SCATTERING BY A BURIED OBJECT IN LOSSY MEDIA

In the previous section, we have introduced an efficient hybrid method for evaluating SFs. As emphasized, the true capabilities of our hybrid meshes and scheme are expected to shine in scenarios involving more intricate media than free space, especially in simulating SFs from buried objects in lossy media. Within the context of our application, focused on simulating airborne radar measurements, this section introduces models from existing literature capable of handling such configurations. We outline our approach to efficiently integrate these models into the finite volume technique. Then, we provide some examples to validate their implementation in the FVTD-UNST scheme and demonstrate the benefits of using locally refined meshes. Finally, we explain and elaborate the adaptation and challenges of using this models in the hybrid FVTD-ST/UNST scheme.

4.1 | Models related to the consideration of the ground

In the simulation of airborne measurements within the context of detecting buried objects, it is imperative to consider various models in our numerical schemes. This is especially essential for the introduction of a plane wave source in the presence of the ground and for the far-field evaluation. Following,[3] the incident field is evaluated by solving a 1-D Maxwell problem in the presence of the bi-medium (air/ground). This is achieved by exploiting invariance in the direction perpendicular to the plane of incidence and introducing a time delay. The general principle is as follows: Field values are obtained numerically via an 1-D auxiliary simulation, carried out along with the main simulation. A smaller time step dt_{1D} is used in the 1-D auxiliary grid for calculating the incident field, ensuring stability. And to conform to the main-grid time spacing, the 3-D time step dt_{3D} must be an odd multiple of the 1-D grid time step: $dt_{3D} = (2M-1)dt_{1D}$ (with M an integer). Updates for 1-D-grid are done in a single main grid update cycle. The 3-D source is updated from 1-D while ensuring correspondence of each field component between the 3-D and 1-D time axes (Figure 8).

Considering the local time stepping in FVTD-UNST, the source update is more complex. Indeed, remember that presence of cell classes with local time stepping means that the global time step of the FVTD-UNST method, corresponding to dt_{3D}, is: $dt_{1D} = 3^{(N-1)}dt_{\min}$ (with $dt_{\min}$ the minimum time step of the UNST-part). In this case, to conform to the main-grid time spacing, it's the minimum time step $dt_{\min}$ that must be an odd multiple of the 1-D grid time step: $dt_{\min} = (2M-1)dt_{1D}$. The 3-D source is updated for each cell class from 1-D while ensuring correspondence of each field component between the 3-D and 1-D time axes. As mentioned earlier, fields for each cell class are computed recursively at each local time step until reaching the global time (Figure 9). The incident field is then introduced using the SF formulation.[1]

Concerning the computation of the far SFs, we should introduced it using a Near- to Far-field transformation in frequency domain, akin to the approach outlined in[19] for the FDTD scheme. This transformation is performed in

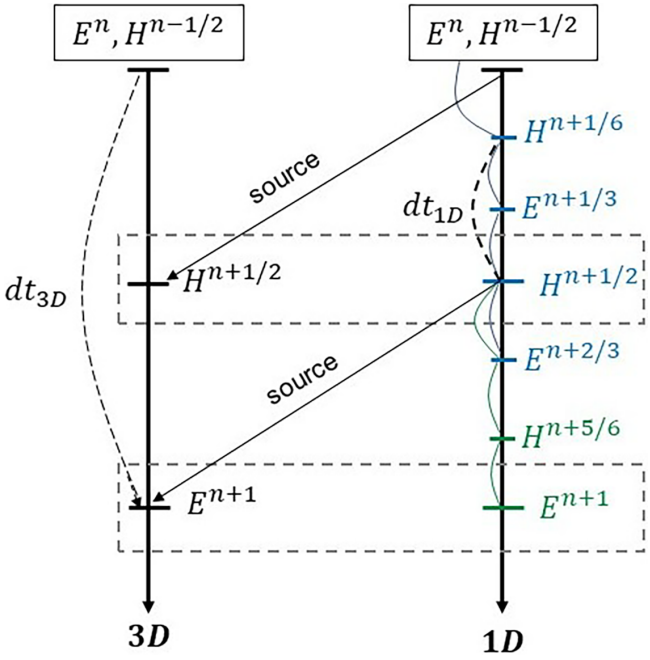

FIGURE 8 Time step reduction in the 1-D auxiliary grid for stability and correspondance between 3-D and 1-D times axes, with $dt_{3D} = 3dt_{1D}$ ($M = 2$).

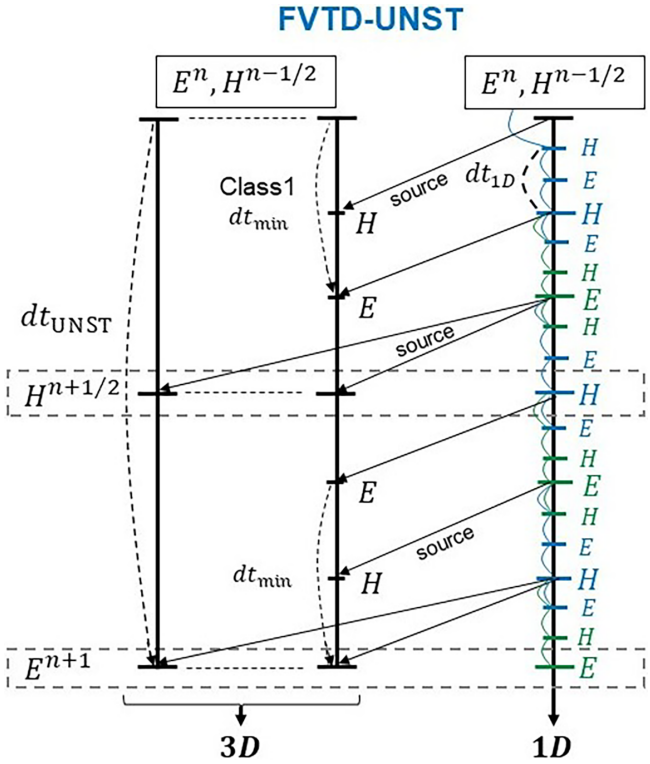

FIGURE 9 Time step reduction in the 1-D auxiliary grid for stability and correspondance between 3-D and 1-D times axes in the UNST-part, for $dt_{\text{UNST}} = 3dt_{\min}$ in presence of two cell classes, and $dt_{\min} = 3dt_{1D}$ ($M = 2$).

frequency domain because, in the presence of a lossy dielectric half-space such as the ground, the Green's functions involved in the computation of the far-field are very difficult to express in the time domain.

Regarding our hybrid method, we choose to implement the Near-to-Far-field transformation in frequency domain, using SFs computed with FVTD-ST scheme, along with the computation of the incident field in the FVTD-UNST

scheme. We initially implement the two models presented here into our FVTD-UNST scheme to establish an FVTD framework able to handle air/ground/object scenarios and utilizing hybrid meshes. However, to fully capitalize on the advantages offered by our hybrid FVTD-ST/UNST scheme within this context, further investigation is required, and adjustments need to be incorporated. The chosen strategy and its associated challenges are elaborated upon in detail in Section 4.3.

4.2 | Numerical examples

In this section, we validate the previously introduced models using our FVTD-UNST method stand-alone, through examples from the literature that feature a cube and a sphere buried in a homogeneous ground. Subsequently, we revisit and adapt the latter to examine and highlight the benefits of using locally refined meshes.

4.2.1 | Validation of the models for ground consideration

Our tests for validation are performed on diffraction problems on a dielectric cube and a dielectric sphere buried in a half-space medium (Figures 10 and 11). Both the objects and the medium are lossy, with relative permittivity values of $\epsilon_c' = 2.9$ and $\epsilon_g' = 3.0$, and conductivity values of $\sigma_c = 0.001669$ and $\sigma_g = 0.003338$, respectively. The time function of the input waveform is a Gaussian pulse defined by: $E_y = A_{\exp}\left(\frac{-(t-t_0)^2}{b^2}\right)$, with $A = 1$, $t_0 = 2.5$ ns and $b = 0.25$ ns. The selected frequency is 600 MHz ($\lambda = 0.5$ m in free space). Following,[2] the computational domain consists of 90^3 cells, each measuring 0.005 m ($\lambda/100$) on a side. Along the z-axis, the lower 60 cells represent the ground, while the upper 30 cells represent free space. We incorporated five PMLs[16] in each direction ($\pm x$, $\pm y$, $\pm z$), adapted to the presence of a lossy dielectric medium. It should be noted that for the cube mesh, only hexahedral cells are used, whereas for the sphere, a hybrid ST/UNST mesh with tetrahedral cells around the object is employed (similar to the one shown in Figure 1).

Figures 12 and 13 present a comparison between the scattered electric fields obtained by Hill[20] and our simulations. Our FVTD results are similar to those of the Reference 20 but slightly higher, with a relative error estimated to be around 8% on average for the cube and 5% for the sphere, based on peak values. We considered this relative error acceptable, taking into account the differences in computational methods and acknowledging that Hill[20] employs the Born approximation, which, according to him, introduces an estimated error of 10% in his calculations. Moreover, under normal incidence conditions ($\theta_i = 0$), our results for the cube also demonstrate agreement with those of a more recent study.[2]

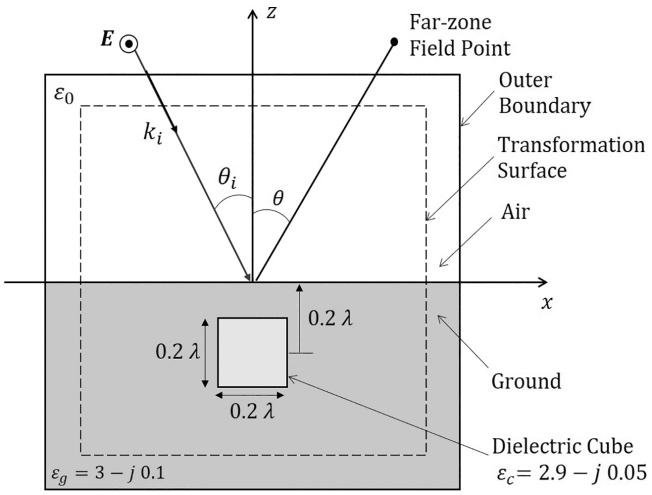

FIGURE 10 Geometry for a lossy dielectric cube buried in a lossy homogeneous ground illuminated by an incident plane wave.

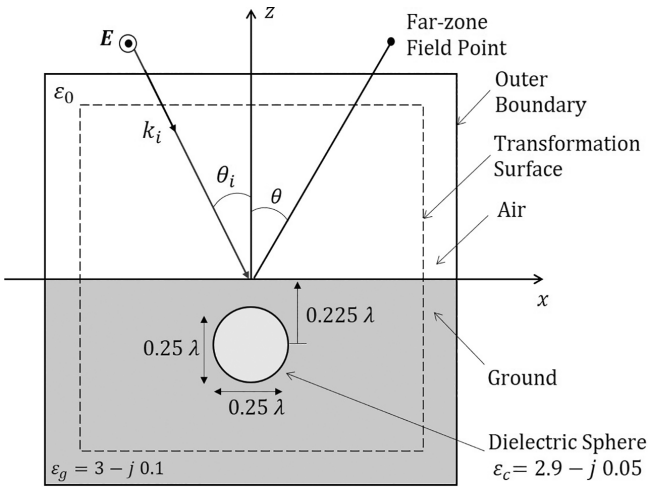

FIGURE 11 Geometry for a lossy dielectric sphere buried in a lossy homogeneous ground illuminated by an incident plane wave.

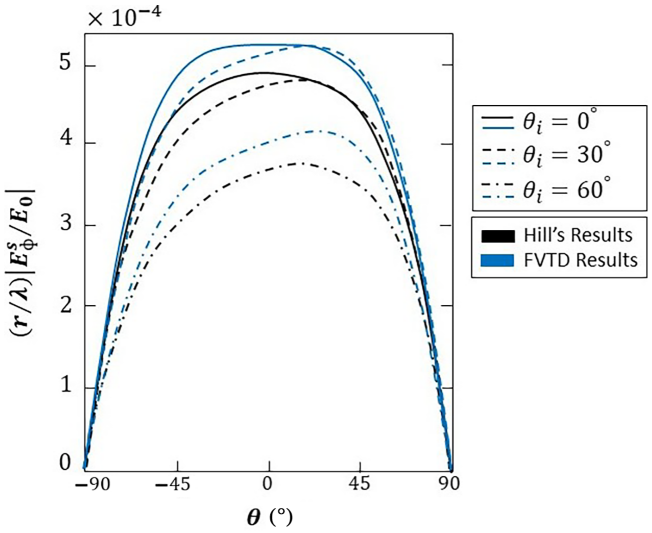

FIGURE 12 The far-zone scattered radiation electric fields from a buried dielectric cube for an *y*-polarized wave at various incidence angles θ_i. Comparison between[20] (black curves) and our simulations (blue curves).

4.2.2 | Locally refined meshes

In this section, we revisit the previous examples. However, instead of using meshes with cells of identical sizes, we employ locally refined hybrid meshes. For both the cube and the sphere, we define two areas: one containing free space and the other containing the ground and the object. The EM wave propagation speed in the ground is given by: $v_g = c_0/\sqrt{\epsilon_g'}$ (with c_0, the wave propagation speed in free space). Given the relative permittivity value of the ground, the wave propagation speed in the ground will be almost two times slower than in free space. Therefore, we choose to maintain a cell edge size of 0.005 m in the ground ($\sim\lambda_g/58$) but to coarsely mesh the part representing free space with cells having an egde size of 0.015 m ($\sim\lambda_g/33$). The dimensions of the computational domain remain unchanged; however, the number of cells in the zone representing free space has been divided by three. Subsequently, we will refer to these new configurations as refined meshes A_{cube} and A_{sphere}. Figure 17, located in Section 4.3, shows an illustration of the cross-section of the mesh A_{sphere}. Figures 14 and 15 show that the results obtained for normal incidence ($\theta_i = 0^\circ$) using refined meshes are very close to those we obtained previously with uniform meshes, and approach those obtained by Hill.[20] Furthermore, when comparing the computation times, the use of the refined meshes A_{cube} and A_{sphere}, significantly reduces the computational costs. Indeed, in both cases, the computational time is reduced by a factor of 1.5. This reduction is partly due to the smaller number of cells to be processed but also thanks to the local time stepping. Indeed,

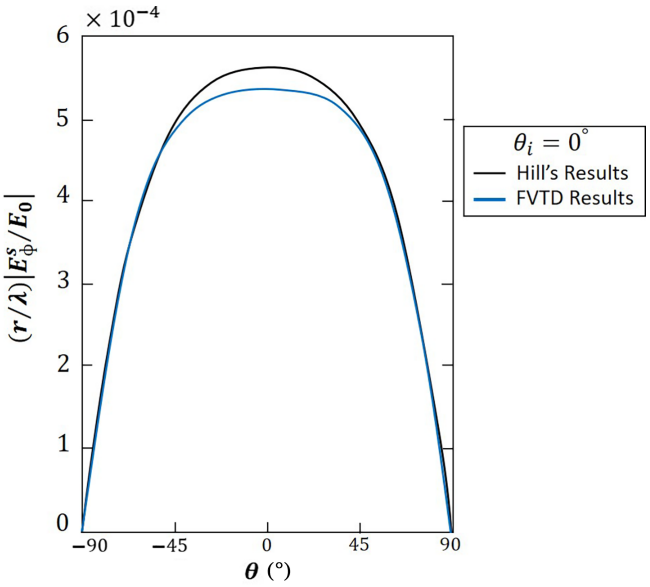

FIGURE 13 The far-zone scattered radiation electric fields from a buried dielectric sphere for an *y*-polarized wave at normal incidence $\theta_i = 0°$. Comparison between[20] (black curve) and our simulations (blue curve).

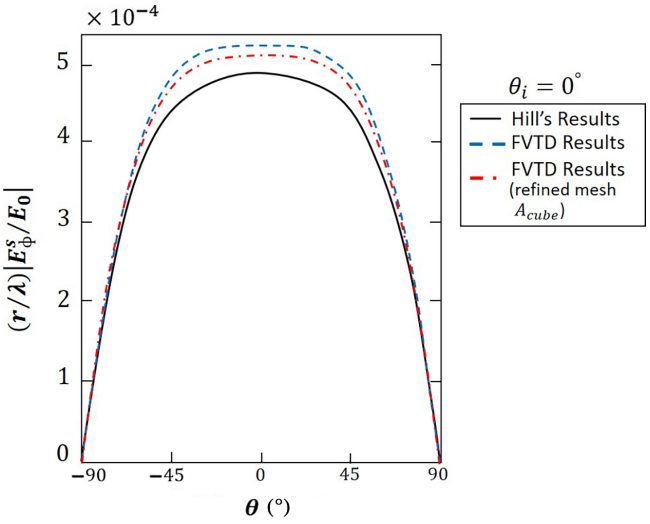

FIGURE 14 The far-zone scattered radiation electric fields from a buried dielectric cube for an *y*-polarized wave at normal incidence angle $\theta_i = 0°$. Comparison between[20] (black curves) and our simulations (blue and red curves).

since two cell domains with significantly different sizes have been established regarding the cube, two cell classes along with their respective local time steps have been defined (Table 5). Thus, the global time step used here ($dt_{\mathrm{UNST}} = 7.4999 \times 10^{-12}$ s) is three times larger than when using the non-refined mesh ($dt_{\mathrm{UNST}} = 2.4999 \times 10^{-12}$ s). Regarding the sphere, the global time step has not changed ($dt_{\mathrm{UNST}} = 4.1897 \times 10^{-12}$ s), since five classes have been defined in both cases (uniform mesh and refined mesh A_{sphere}); only the number of cells assigned to each class has evolved due to the smaller number of cell in the zone corresponding to the air (Table 6).

These examples demonstrate the possibility of using a mesh with two different cell size areas: one for the air and another for the ground and object, thereby reducing computational cost. Refined hybrid meshes with more than two zones are also conceivable when necessary.

To conclude, let's consider one final example that of a cube with a higher relative permittivity compared with that of the ground. As the relative permittivity of a dielectric material in the computational scene increases, finer meshing

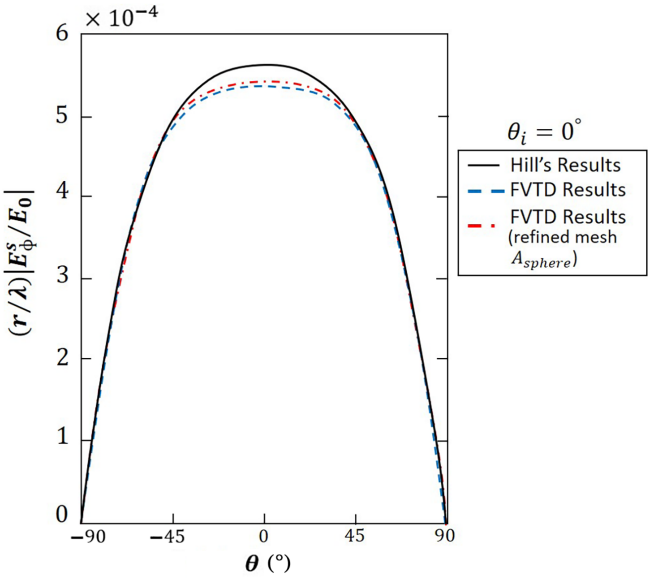

FIGURE 15 The far-zone scattered radiation electric fields from a buried dielectric sphere for an *y*-polarized wave at normal incidence $\theta_i = 0°$. Comparison between[20] (black curve) and our simulations (blue and red curves).

TABLE 5 Distribution of mesh cells into two classes for FVTD-UNST computations on the refined mesh A_{cube}, in the case of the dielectric cube, and their corresponding local time steps ($dt_{\text{UNST}} = 7.4999 \times 10^{-12}$ s).

Class	Number of cells per class	dt_{loc}
1	686 664	2.4999×10^{-12} s
2	13 872	7.4999×10^{-12} s

TABLE 6 Distribution of mesh cells into five classes for FVTD-UNST computations on the uniform mesh and the refined mesh A_{sphere}, in the case of dielectric sphere, and their corresponding local time steps ($dt_{\text{UNST}} = 4.1897 \times 10^{-12}$ s).

Class	dt_{loc}	Number of cells per class Uniform mesh	Number of cells per class Refined mesh A_{sphere}
1	5.1725×10^{-14} s	4	4
2	1.5517×10^{-13} s	16	12
3	4.6552×10^{-13} s	17 039	17 149
4	1.3966×10^{-12} s	1 003 896	690 573
5	4.1897×10^{-12} s	2	13 874

of the material becomes necessary. Since only the permittivity of the object has changed, we can consider only reducing the mesh size corresponding to it without modifying those of the ground and free space. The cube now has a permittivity value ϵ_c' of 12.0 instead of 2.9. To accommodate this new high permittivity material, we halved the cell size representing the cube (the cells now have edges of 0.0025 m $\sim\lambda_g/58$). Subsequently, we will refer to this configuration as refined mesh B_{cube}. Before performing the computation, we ensured that using this new refined mesh while keeping ϵ_c' at 2.9 would yield the same results as before, which indeed proved to be the case.

Figure 16 presents the result obtained with $\epsilon_c' = 12.0$ and the refined mesh B_{cube} with three distinct zones (the cube, the ground and free-space), in the case of normal incidence. Comparing the results obtain with $\epsilon_c' = 2.9$ (Figure 15) and with $\epsilon_c' = 12.0$ (Figure 16), we observe that the amplitude of the radiated field is higher when the permittivity contrast between the ground and the object is more significant. One possible explanation for this observation is that the higher the contrast between the ground and the object, the more pronounced the object's response is.

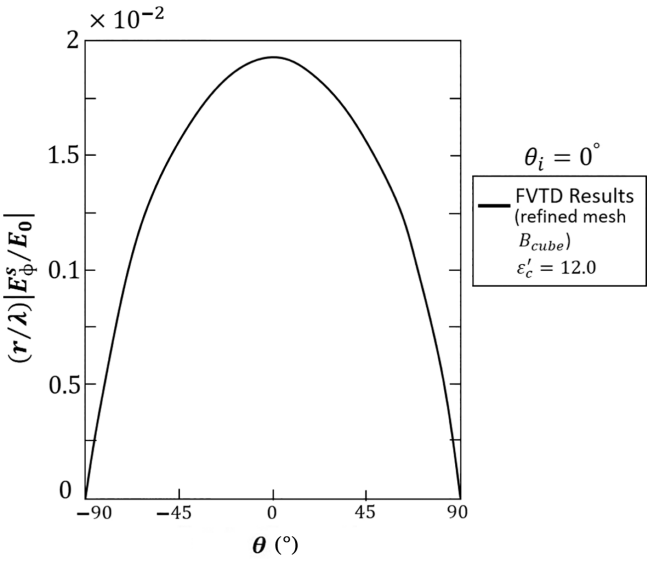

FIGURE 16 The far-zone scattered radiation electric fields from a buried dielectric cube for an *y*-polarized wave at normal incidence angle $\theta_i = 0°$.

Treating this scenario with a uniform mesh increases the number of cells by a factor of 8.8. Consequently, for identical solutions, this results into an increase of this order of magnitude in computation time compared with the simulation using the refined mesh B_{cube}. The gain obtained thanks to refinement is substantial. Once again, this is due to the reduction in the number of cells to represent free space and the use of local time-stepping (two classes of cells: one for free space and one for the ground and object), similar to the previous example.

In these examples, we have demonstrated the advantages of using locally refined meshes over uniform meshes, with our FVTD-UNST method, for handling complex scenarios involving multilayered media with varying propagation velocities and objects with diverse permittivities. Instead of meshing the entire domain based on the highest permittivity value, this approach enables a fine mesh only in necessary areas by adjusting the cell size according to the specific dielectric properties of each object or medium in the computational scene.

An additional advantage of employing locally refined zones lies in the ability to implement a local time stepping, thereby reducing computational costs.

The last example, featuring rectangular shapes, is certainly not the most relevant for effectively showcasing or capitalizing on our FVTD-UNST associated with locally refined hybrid meshes. Indeed, for this type of configuration the FDTD method is more suitable and remains more efficient in terms of computation time. However, the future implementation of the hybrid FVTD-ST/UNST method on such meshes will attenuate this performance difference, as we have seen in the case of the free space example in Section 3.4. Moreover, the combination of the hybrid FVTD-ST/UNST method with hybrid-refined meshes should surpass the FDTD approach, in terms of accuracy and computational cost, in the presence of more complex scenarios involving curved geometries.

4.3 | Hybrid FVTD-ST/UNST approach for multiple ST- and UNST-zones

In the previous subsections, we validated the models required to consider scenarios involving objects buried in homogeneous grounds, first introducted in the stand-alone FVTD-UNST scheme. We have also demonstrated through the previous examples, that in the presence of multiple mediums with different propagation velocities, our stand-alone FVTD-UNST approach associated with locally refined hybrid meshes present real advantages. However, there is still-room for performance improvement by adapting and utilizing the hybrid FVTD-ST/UNST solution for multiple ST- and UNST-zones.

Let's illustrate our strategy considering an air/ground/object scenario where we employ a hybrid ST/UNST mesh, processed by our hybrid FVTD-ST/UNST solver. The air and the ground are two distinct dielectric zones. We can choose to employ either a hybrid ST/UNST mesh in which there is only one ST-area with a constant spatial step

encompassing both air and ground, or a locally refined hybrid ST/UNST mesh with two ST-areas of different mesh sizes tailored to the distinct propagation speeds.

Considering the first possibility, we are constrained to use the smallest spatial step, adapted to the medium with the slowest propagation speed, for the entire ST-zone. The two distinct propagation speeds (in air and ground) imply two distinct time steps. Thus, we end up with a Cartesian mesh with a constant spatial step and two temporal steps. If the approach described in Section 3 suggests adopting the smaller of these time steps as the global time step for the ST-part (dt_{ST}), this is clearly not the most judicious approach. Despite restricting the use of the FVTD-UNST solver only to UNST-parts, using the same minimal time step for all ST-parts is not very efficient. Therefore, to consider the two time steps, it is necessary to introduce a local time stepping strategy similar to the one employed in the FVTD-UNST scheme into the FVTD-ST technique. The challenge lies in defining time meeting points between the two schemes. To accomplish this correctly, we propose defining an equal number of classes with identical local time steps for all schemes, with time meeting points set at the time steps of the largest class. This requires each scheme to know the minimum of the maximum time step of all schemes (FVTD-ST and FVTD-UNST) as well as the minimum of the minimum time step of all schemes.

By adopting this approach, the computational principle is similar to a global stand-alone FVTD-UNST computation, in which all volumes are seen as unstructured. However, with the advantage of locally using simpler, less costly FVTD-ST calculations, making the hybrid solver more efficient than the standalone FVTD-UNST approach on the same mesh. Nevertheless, an obvious improvement from a mesh perspective can still be made, which is to not use the same spatial step for the entire ST-zone, in order to limit over-meshing.

Now, let's consider the use of a locally refined hybrid mesh. The air and the ground are represented by two Cartesian areas with their respective constant spatial steps tailored to the propagation speeds. Generally, the air zone should have a larger mesh size, as discussed in examples in Section 4.2.2. An evident advantage here is the reduction of cells in the air zone, thanks to the use of locally refined meshes. At the air/ground interface, cells with more than six faces may be present, thus becoming part of the UNST-portion (Figure 17). Overall, we would then have two ST-zones (air and ground) and one UNST-zone encompassing the UNST cells around the object as well as those at the air/ground interface.

To integrate this into the hybridization strategy, the idea is to consider hybridization between three schemes: two FVTD-ST and one FVTD-UNST. The time meeting points would then be defined via local time stepping strategy, as presented previously. This should present no more difficulty than the initial FVTD-ST/UNST hybrid strategy considering only one ST-zone and one UNST-zone.

This latter approach, which should prove to be much more effective than the stand-alone FVTD-UNST scheme on locally refined hybrid meshes and then the hybrid FVTD-ST/UNST strategy on a "simple" hybrid mesh (only one

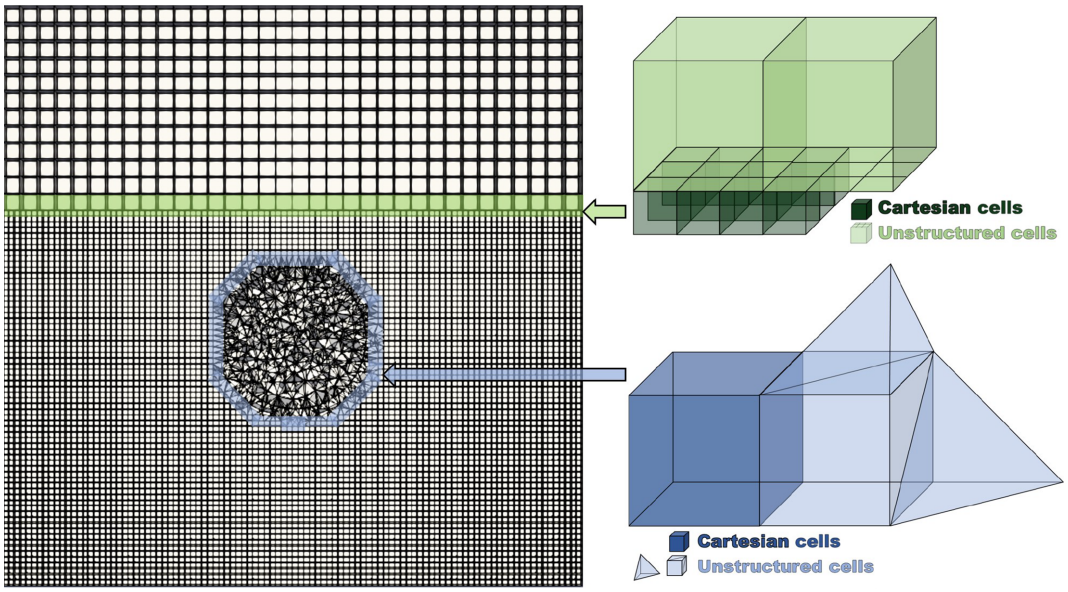

FIGURE 17 Cross section of a Hybrid ST/UNST mesh and cell hybridization interfaces between Cartesian and unstructured zones.

ST-zone and one UNST-zone), is still under development. Our aim is for our hybrid method to surpass the efficiency of the FDTD method, in particular by optimizing the number of iterations per operation in the FVTD-ST scheme.

5 | CONCLUSION

In this paper, we focused on simulating the RCS of buried objects illuminated by an airborne radar system. Due to the geometry of the objects and the environments that could be considered, we have proposed a hybrid approach in terms of meshes associated with a hybrid finite volume solution in terms of numerical schemes. In particular, we have demonstrated the efficiency of this approach with simple examples, such as calculating the RCS of a PEC sphere in free space. Additionally, we have shown that reducing the number of cells in the computational domain using refined meshes, significantly decreases computation time, as illustrated in the case of computating SFs by a dielectric object buried in a ground. The highlighted advantages include the precise consideration of geometries (curved surfaces), the possibility of using locally refined meshes, and employing finite volume schemes adapted to both ST- and UNST-parts in a stable hybrid solution. Our future work will revolve around improving the hybrid scheme, with a particular emphasis on enabling multiple Cartesian and unstructured areas with different local refinements, as well as optimizating the number of operations per iteration in the FVTD-ST scheme.

ACKNOWLEDGEMENTS

This work was supported by a grant from the Agence de l'Innovation de Défense (AID) and the Office National d'Etudes et de Recherches Aérospatiales (ONERA).

DATA AVAILABILITY STATEMENT

The data that support the findings of this study are available from the corresponding author upon reasonable request.

ORCID

Lisa-Marie Mazzolo https://orcid.org/0009-0007-1127-708X

REFERENCES

1. Demarest K, Plumb R, Huang Z. FDTD modeling of scatterers in stratified media. *IEEE Trans Antennas Propag*. 1995;43(10):1164-1168. doi:10.1109/8.467657
2. Demarest K, Huang Z, Plumb R. An FDTD near- to far-zone transformation for Scatterers buried in stratified grounds. *IEEE Trans Antennas Propag*. 1996;44(8):1150-1157. doi:10.1109/8.511824
3. Capoglu I, Smith G. A Total-field/scattered-field plane-wave source for the FDTD analysis of layered media. *IEEE Trans Antennas Propag*. 2008;56:158-169. doi:10.1109/TAP.2007.913088
4. Yee S. Numerical solution of initial boundary value problems involving Maxwell's equations in isotropic media. *IEEE Trans Antennas Propag*. 1966;14(3):302-307. doi:10.1109/TAP.1966.1138693
5. Taflove A, Hagness C. *Computational Electrodynamics: the Finite-Difference Time-Domain Method*. 2nd ed. Artech House; 2000.
6. Yee S, Chen S. The finite-difference time- domain (FDTD) and the finite-volume time-domain (FVTD) methods in solving Maxwell equation. *IEEE Trans Antennas Propag*. 1997;45(3):354-363. doi:10.1109/8.558651
7. Bonnet P, Ferrieres X, Issac F, et al. Numerical modeling of scattering problem using a time domain finite volume method. *J Electromag Waves Appl*. 1997;11(8):1165-1189. doi:10.1163/156939397X01070
8. Firsov D, LoVetri J, Jeffrey I, Okhmatovski V, Gilmore C, Chamma W. High-order FVTD on unstructured grids using an object-oriented computational engine. *Appl Comput Electromag Soc J*. 2007;22(1):71-82.
9. Edelvik F, Ledfelt G. A comparison of time-domain hybrid solvers for complex scattering problems. *Int J Numer Model: Electron*. 2002; 15(5–6):475-487. doi:10.1002/jnm.463
10. Ferrieres X, Parmantier JP, Bertuol S, Ruddle R. Application of a hybrid finite difference/finite volume method to solve an automotive EMC problem. *IEEE Trans Electromagn Compat*. 2004;46(4):624-634. doi:10.1109/TEMC.2004.837837
11. Geuzaine C, Remacle JF. Gmsh: a three-dimensional finite element mesh generator with built-in pre- and post-processing facilities. *Int J Numer Methods Eng*. 2009;79(11):1309-1331.
12. Bonnet F, Bostan M, Fezoui L. Étude d'une classe de [bêta-gamma] schémas en formulation volumes finis pour des problèmes hyperboliques. 1997 https://inria.hal.science/inria-00073400
13. Piperno S, Remaki M, Fezoui L. A centered second-order finite volume scheme for the heterogeneous Maxwell equations in three dimensions on arbitrary unstructured meshes. 2001 https://inria.hal.science/inria-00072461
14. Rao M. Timdes Domain Electromagnetics. Auburn, AL: Department of Electrical Engineering, Auburn University. 1999.

15. Van Leer B. Towards the ultimate conservative difference scheme V. A second-order sequel to Godunov's method. *J Comput Phys*. 1979; 32:101-136. doi:10.1016/0021-9991(79)90145-1
16. Berenger JP. A perfectly matched layer for the absorption of electromagnetic waves. *J Comput Phys*. 1994;114(2):185-200. doi:10.1006/jcph.1994.1159
17. Bassem M. *Radar Systems Analysis and Design Using MATLAB*. 2nd ed. Chapman and Hall/CRC; 2005.
18. The MathWorks I. Radar Toolbox version: 23.2 (R2023b). 2023 https://www.mathworks.com
19. Martin T, Pettersson L. FDTD time domain near- to far-zone transformation above a Lossy dielectric half-space. *Appl Comput Electromag Soc J*. 2001;16(1):45-52.
20. Hill DA. Electromagnetic scattering by buried objects of low contrast. *EEE Trans Geosci Remote Sens*. 1988;26(2):195-203. doi:10.1109/36.3021

How to cite this article: Mazzolo L-M, Ferrieres X. Hybrid Cartesian/unstructured numerical method for efficient evaluation of scattered fields: Application to buried object detection from airborne platforms. *Int J Numer Model*. 2024;37(4):e3270. doi:10.1002/jnm.3270